








Anomalous atomic fluctuations in the local structure around Mn of (Zn, Sn, Mn)As₂ thin filmsH. Kizaki ^{1,2,3,*} K. Hayashi ^{4,5,†} Cong Lu,^{4,‡} N. Happo ⁶ S. Hosokawa ⁷ S. Hidaka ⁸ S. Hayashi,⁹ M. Suzuki ¹⁰ and N. Uchitomi ^{2,9}¹Graduate School of Engineering, Osaka University, Suita, Osaka 565-0871, Japan²Center for Spintronics Research Network, Osaka University, Toyonaka, Osaka 560-8531, Japan³Elements Strategy Initiative for Catalysts and Batteries, Kyoto University, Katsura, Kyoto 615-8520, Japan⁴Department of Materials Science and Engineering, Nagoya Institute of Technology, Nagoya 466-8555, Japan⁵Japan Synchrotron Radiation Research Institute, SPring-8, Kouto, Sayo, 679-5198, Japan⁶Graduate School of Information Sciences, Hiroshima City University, Hiroshima 731-3194, Japan⁷Institute of Industrial Nanomaterials, Kumamoto University, Kumamoto 860-8555, Japan⁸Graduate School of Science, Osaka University, Toyonaka, Osaka 560-8531, Japan⁹Department of Electrical Engineering, Nagaoka University of Technology, Nagaoka 940-2188, Japan¹⁰School of Engineering, Kwansai Gakuin University, Sanda, Hyogo 669-1330, Japan

(Received 28 May 2021; revised 24 August 2021; accepted 27 July 2022; published 29 August 2022)

Local atomic structures around Mn in (Zn, Sn, Mn)As₂ thin films grown on InP (001) substrates were studied using x-ray fluorescence holography. The reconstructed three-dimensional atomic images showed that the addition of Mn resulted in further distortions of the As sublattice from the pure sphalerite ZnSnAs₂. The first-principles calculations showed that the further distortion could be attributed to the shortening of the Mn-As bond length induced by the *p-d* exchange mechanism, which mediates the ferromagnetism in this material. In addition, we found that the positional fluctuation of the cations was maximized at the second nearest neighbor cation shell from detailed analysis of the atomic images. This anomaly in the fluctuation could be explained by the calculated forces acting on the cations.

DOI: [10.1103/PhysRevB.106.064434](https://doi.org/10.1103/PhysRevB.106.064434)**I. INTRODUCTION**

Ferromagnetic (FM) semiconductors have been considered as one of the promising candidates for the development of spintronic devices such as a spin field effect transistors, where both charge and spin degrees of freedom are expected to be controllable to achieve functionality in devices [1,2]. Over the last two decades, most of the fundamental and applied studies have been focused on doped III-V semiconductors such as (Ga, Mn)As, where one of the key issues is having FM properties exhibited at room temperature or higher [3–7]. In recent years, another family of FM semiconductors based on the structure of the Mn-doped ternary semiconductors has been reported; these include Mn-doped II-IV-V₂ compounds (which are referred to as II-IV-V₂: Mn or (II, IV, Mn)V₂), such as CdGeP₂: Mn and ZnSnAs₂: Mn [8–10]. These compounds have more advantages over doped III-V compounds, including the ability to control the charge doping and spin doping in two different cation sites.

In the family of II-IV-As₂ compounds, the semiconductor ZnSnAs₂, with a band gap of 0.73 eV in the bulk chalcopyrite form, possesses special advantages for room-temperature ferromagnetism [8–10] and epitaxial thin film lattice matching

with InP substrates [9,10]. From a technological point of view, these attractive characteristics are suitable for realizing a building block in spintronic devices. The magnetic properties of (Zn, Sn, Mn)As₂ have been studied fundamentally by macroscopic techniques such as superconducting quantum interference device (SQUID) magnetometry and Hall measurements, which do not probe the local-structure scale distribution of Mn dopants. Here, x-ray fluorescence holography (XFH) [11] was employed as a three-dimensional (3D) imaging technique to explore the local atomic structures inside the unit cell of ZnSnAs₂ [12].

In the recent developments in 3D imaging techniques, XFH has been proven as a powerful tool for various types of structural characterization of crystals, especially in clarifying the local lattice distortions around specific elements [13], the formation of local clusters [14], and local structure in quasicrystal [15]. These results are not easily obtained by conventional diffraction or x-ray absorption fine structure (XAFS) experiments. Another difficulty in the structural characterization of crystals is the quantitative determination of crystal forms in disordered systems. In a previous report, we measured the 3D local structure of (Zn, Sn, Mn)As₂ thin films using XFH [16], and found that this technique can be a very powerful tool for epitaxially grown thin films, as well as bulk crystals despite the very small number of Mn atoms. However, we also recognized that improvements in the signal to noise (SN) ratio will be necessary.

Recently, we have successfully carried out the XFH measurements to understand the local atomic structure around Zn

*kizaki@eng.osaka-u.ac.jp

†hayashi.koichi@nitech.ac.jp

‡Present address: Synchrotron Radiation Research Center, Hyogo Science and Technology Association, Tatsuno, Hyogo 679-5165, Japan.

atoms in the host ZnSnAs_2 thin films after some improvements in the measurement system [12]. The reconstructed 3D atomic images show that the crystal structure of the ZnSnAs_2 thin film is mainly of the sphalerite structure. A large distortion of the As sublattice is observed, whereas the positions of the Zn/Sn atoms are relatively stable. The analysis of the data indicates that the As layers serve as a buffer and relax the strain caused by the random occupation of cation atoms.

We have conducted further investigations on the basis of previous work to learn details of the local atomic structure around Mn atoms in $(\text{Zn, Sn, Mn})\text{As}_2$ thin films by XFH measurements with an improved SN ratio. In this article, we report detailed analyses of the reconstructed atomic images, and subsequently describe a theoretical approach using first-principles calculations to verify the anomaly in the atomic fluctuations observed by XFH. The large As-sublattice distortion in $(\text{Zn, Sn, Mn})\text{As}_2$ is also discussed in terms of the ferromagnetism.

II. EXPERIMENTAL AND CALCULATION PROCEDURE

A. Sample preparation

The sample for XFH measurements was prepared using molecular beam epitaxy (MBE). A 500 nm thick $(\text{Zn, Sn, Mn})\text{As}_2$ thin film was epitaxially grown on semi-insulating InP (001) substrates after the growth of a 16 nm thick ZnSnAs_2 buffer layer, without any indication of a secondary-phase formation. The substrate temperature was set to 300°C. The crystalline structure of the grown films was characterized by conventional high-resolution x-ray diffraction (HRXRD) measurement. SQUID measurement showed that the films exhibited room-temperature ferromagnetism with a Curie temperature of $T_C \sim 310$ K [9]. Details of the growth process and conditions, the structure, and the magnetic properties were described elsewhere [10,12]. At the present doping level, we could not explicitly observe hexagonal MnAs phase-segregated regions throughout the XRD measurements. It should be emphasized that the ZnSnAs_2 thin films are nearly lattice matched with the InP (001) substrates, resulting in the formation of a smooth interface and the suppression of misfit dislocations. Electron probe microanalysis (EPMA) measurements revealed that the composition of the sample was $(\text{Zn}_{50.2}, \text{Sn}_{44.8}, \text{Mn}_{5.0})\text{As}_2$. We note that Mn atoms were preferentially substituted for Sn atoms.

B. X-ray fluorescence holography

The XFH measurements in inverse mode [17] were carried out at beamline BL39XU of SPring-8, Japan. The sample surface size was 10×10 mm². The Mn $K\alpha$ fluorescent x rays from $(\text{Zn, Sn, Mn})\text{As}_2$ were collected using an avalanche photodiode detector via a cylindrical graphite energy analyzer. The measurements were performed by rotating two axes of the sample, the incident angle $0^\circ \leq \theta \leq 75^\circ$ in steps of 1.0° , and the azimuthal angle $0^\circ \leq \phi \leq 360^\circ$ in steps of 0.25° . The average intensity of the fluorescent x rays at each pixel is about 15 000 counts. The holograms for $(\text{Zn, Sn, Mn})\text{As}_2$ were recorded with nine different incident x-ray energies: 6.8-10.8 keV in steps of 0.5 keV. Details of the setup are given elsewhere [12]. One of the aims of the present work

was the quantitative determination of atomic fluctuations, as in our past studies. Holographic oscillation data were obtained by subtracting the background from the fluorescent x-ray intensities and normalizing them by the incident x-ray intensities. The statistical improvement of the holographic data was carried out by the symmetrization of the raw data using the crystallographic symmetry of the sphalerite crystal structures (space group: $F\bar{4}3m$) and the measured x-ray standing wave (XSW) lines. The 3D atomic images of the samples around Mn were reconstructed from multiple-energy holograms using Barton's algorithm [18].

C. DFT calculations

To understand the electronic structure and magnetic properties in $(\text{Zn, Sn, Mn})\text{As}_2$, we employed density functional theory (DFT) implementations: A plane-wave pseudopotential method (QUANTUM ESPRESSO) [19]. We used the generalized gradient approximation (GGA) in the Perdew-Burke-Ernzerhof (PBE) parametrization for the exchange correlation functional. Ultrasoft pseudopotentials were used, where $3d$ and $4s$ states are considered for Zn with 12 electrons; $4d$, $5s$, and $5p$ states are considered for Sn with 14 electrons; $3s$, $3p$, $3d$, $4s$, and $4p$ states are considered for Mn with 13 electrons; and $4s$ and $4p$ states for As with 5 electrons. We employed the pseudopotentials for Zn, Sn, Mn, and As generated by scalar-relativistic calculations, and non-linear core corrections were included in the pseudopotentials for Sn, Mn, and As. Lattice constants and internal parameters of a chalcopyrite structure were fully optimized using a point of departure from the experimental lattice parameters $a = 5.853$ Å, $c = 11.70$ Å, $c/a = 2.0$, and $u = 0.23$ in terms of the primitive unit cell [20]. All the atomic positions were also fully optimized until the total of the absolute values of the force vectors for all components was smaller than 1×10^{-4} Ry/a.u. via the Broyden, Fletcher, Goldfarb, and Shanno-based (BFGS) method [21]. The Gaussian broadening method was exploited to calculate the density of states (DOS). Brillouin-zone integration was carried out using $6 \times 6 \times 6$ Monkhorst-Pack k -point grids for $2 \times 2 \times 1$ chalcopyrite ZnSnAs_2 supercells, as shown in the Supplemental Material [22] (see Fig. S1). Kinetic-energy cutoffs of 40 Ry (wave functions) and 400 Ry (charge density) were used for the smooth part of the electronic wave functions and the augmented electron density, respectively.

In the present paper, we do not use the DFT + U approach since it is adequate to obtain qualitative explanations for the experimental results in this material [23,24]. Here, we assume the chalcopyrite $\text{Zn}(\text{Sn, Mn})\text{As}_2$ system to distinguish the influence of selective doping sites and to eliminate antiferromagnetic (AFM) systems already reported in $(\text{Zn, Mn})\text{SnAs}_2$ [23]. In fact, MBE-grown $(\text{Zn, Sn, Mn})\text{As}_2$ thin films exhibit preferred substitutions of Sn atoms by Mn [25]. In addition, sphalerite-chalcopyrite mixed structure is also observed in the $(\text{Zn, Sn, Mn})\text{As}_2$ [25]. For these reasons, the locally ordered chalcopyrite structure may exist in sphalerite $(\text{Zn, Sn, Mn})\text{As}_2$, even if XFH could not detect it. Therefore, to narrow down the discussion, here we use the ferromagnetic cluster model of the chalcopyrite structure, in which Mn is substituted at the Sn site. The total energy difference as a

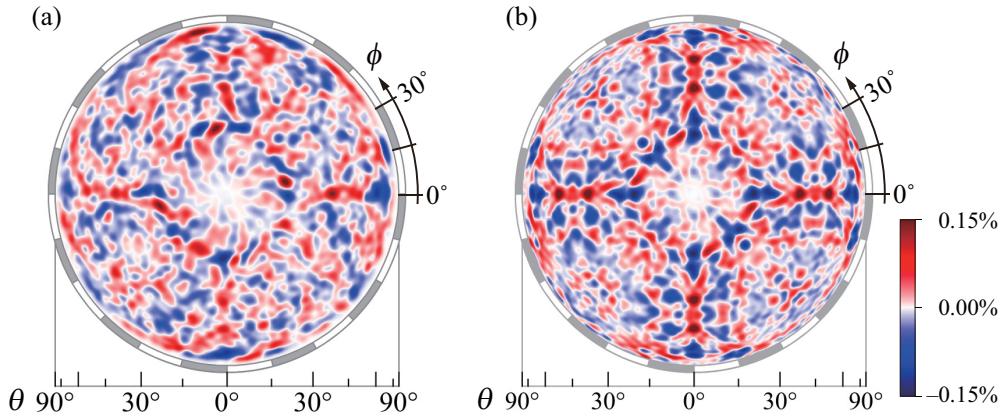


FIG. 1. Mn $K\alpha$ XFH of (Zn, Mn, Sn)As₂ thin films (a) before and (b) after the symmetrization with the space group of $F\bar{4}3m$. The hologram in (b) was extended to a full sphere. The hologram was recorded at 6.8 keV. (a) The radial and angular directions indicate θ and ϕ , respectively. The holograms were Gaussian convoluted with the angular width of 2.8°.

function of the distance between Mn pairs in the unit cell was calculated to link the XFH images and FM properties in Zn(Sn, Mn)As₂. The energy difference between total energies for the AFM state, E_{AFM} , and that for the FM state, E_{FM} , were calculated, where $\Delta E = E_{AFM} - E_{FM} > 0$, which means that the FM state is more stable than the AFM state.

To evaluate the amplitudes of the fluctuations estimated from the XFH images, we focused on the forces acting on cations of interest. When the calculated forces adequately converged, the force at a cation of interest should correspond to a driving force giving rise to the fluctuation from the original position. Therefore, these calculated forces enable us to evaluate the broadening of the XFH images. The forces were calculated for positionally fixed Mn, Zn, and Sn atoms at each shell for both FM and AFM states via the BFGS method after structural optimization [21].

At first, we prepared the same simulation box, as shown in the Supplemental Material [22] (see Fig. S1). Then all the atomic positions were fully optimized under a positionally fixed condition of the atom of interest for both FM and AFM states. Finally, we assessed the respective forces of the Mn- X ($X = Mn_{FM}, Mn_{AFM}, Zn$, and Sn) at each shell.

III. EXPERIMENTAL RESULTS

Figure 1 shows the measured hologram at an incident x-ray energy of 6.8 keV. Small holographic undulations of 0.15% are observed in the displayed pattern, which was low-pass filtered by Gaussian convolution for visibility. A rough twofold symmetry can already be seen in the pattern in Fig. 1(a) even before the symmetry operation. Since the statistics of the symmetrized holograms in Fig. 1(b) was sufficient enough to reconstruct real-space images, 3D atomic images were reconstructed using Barton's algorithm by superimposing the holograms with different incident x-ray energies, which can highly suppress the false twin images produced from the Fourier transform of single energy holograms.

Figure 2 shows the resulting atomic images of the (001) plane at $z = 0.0$ and 2.94 \AA for cation planes and 1.47 and 4.41 \AA for anion planes, which were optimally reconstructed around the central Mn atom obtained from the experimental

hologram. The atomic images from this quaternary system seem to be more complicated than the ternary systems ZnSnAs₂ [12], InGaSb [26], GeMnTe [27], and ZnMnTe [28] previously measured by XFH. The As atomic images are fairly visible up to the third anion shell within the sublattice distortion, while the cation images exhibited similar positional fluctuations that were also observed in the atomic images of the (Zn, Sn)As₂ thin film, both of which can be explained by the large fluctuation of the As sublattice within the sphalerite structure [12]. The large sublattice distortion suggests twisting of the cation-containing As (C-As) tetrahedra. From the present results of the XFH measurements, we can see the middle-range local structure around a Mn atom up to several nanometers.

It is worth noting that magnetic secondary phases may occasionally be observed in the magnetic films using XFH. In a previous work on FM rutile Ti_{0.95}Co_{0.05}O₂ films, the local atomic structures around Co were investigated by XFH [29]. The XFH measurements revealed the presence of Co suboxide clusters in rutile Ti_{0.95}Co_{0.05}O₂. From this experiment, the XFH measurements proved that the magnetic clustering and secondary phases can explicitly be observed in magnetic films when magnetic clusters, such as the Co suboxide structures, exist in the film.

On the other hand, XFH experiments revealed that Ge_{0.6}Mn_{0.4}Te grown on a BaF₂ substrate, one of the IV-VI diluted magnetic semiconductors, is a substitutional alloy without any different clusters such as Mn_xGe_{1-x} and Mn₅Ge₃ [27]. The XFH images around Mn atoms show distinct NaCl-type atomic configurations [27]. It was suggested that preserving the local arrangement of octahedral O_h symmetry around the Mn atoms may be related to FM behavior at relatively high temperatures. From these results, the reconstructed images should appear at different sites if clusters such as secondary phases are present in the sample. In the present work, the presence of the magnetic clusters, such as hexagonal MnAs, were not observed for (Zn, Sn, Mn)As₂ thin films.

From these atomic images, we analyzed the amount of positional fluctuations in the cation and anion sublattices. Using the reconstructed atomic images of the (Zn, Sn, Mn)As₂ and the reference ZnSnAs₂ thin films [12], the image intensities

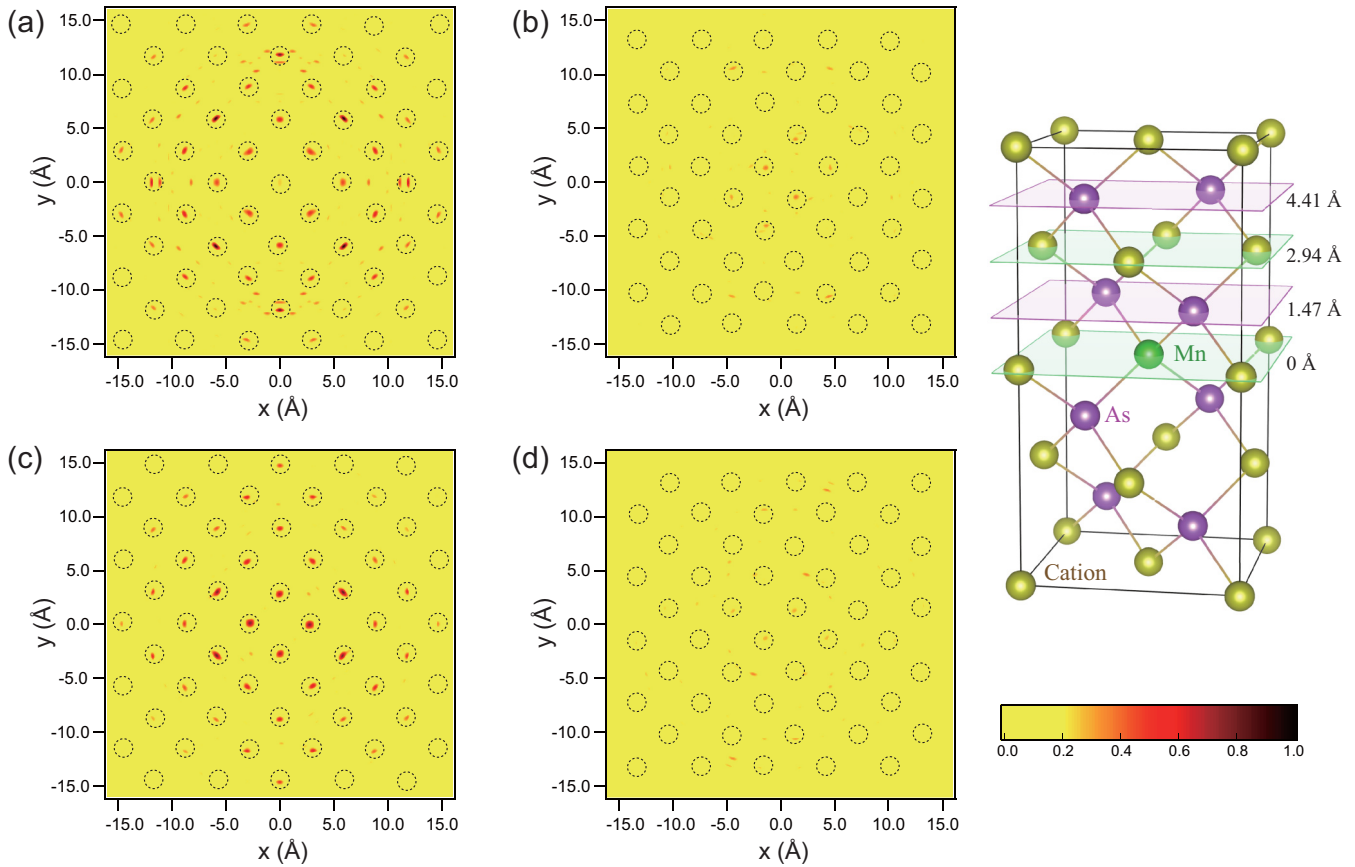


FIG. 2. Atomic images around Mn obtained from experimental holograms on the (001) plane. (a), (c) indicate, respectively, $z = 0.0$ and 2.94 \AA for cation planes. (b), (d) indicate, respectively, 1.47 and 4.41 \AA for anion planes. The inset shows a schematic diagram of $(\text{Zn, Sn, Mn})\text{As}_2$ with sphalerite structure to indicate the XFH image planes.

are plotted as a function of the distance from the central Mn and Zn atom in Figs. 3(a) and 3(b), respectively. The ZnSnAs_2 data used here are the same as those of Fig. 7 in Ref. [12]. In principle, the atomic image intensity is proportional to the atomic number. Therefore, the intensities of

anion images were normalized with respect to the atomic number of As, and the intensities of the cation images were normalized with respect to the fractional averages of the Mn, Zn, and Sn atomic numbers for $(\text{Zn, Sn, Mn})\text{As}_2$ and ZnSnAs_2 , respectively. Furthermore, the atomic image inten-

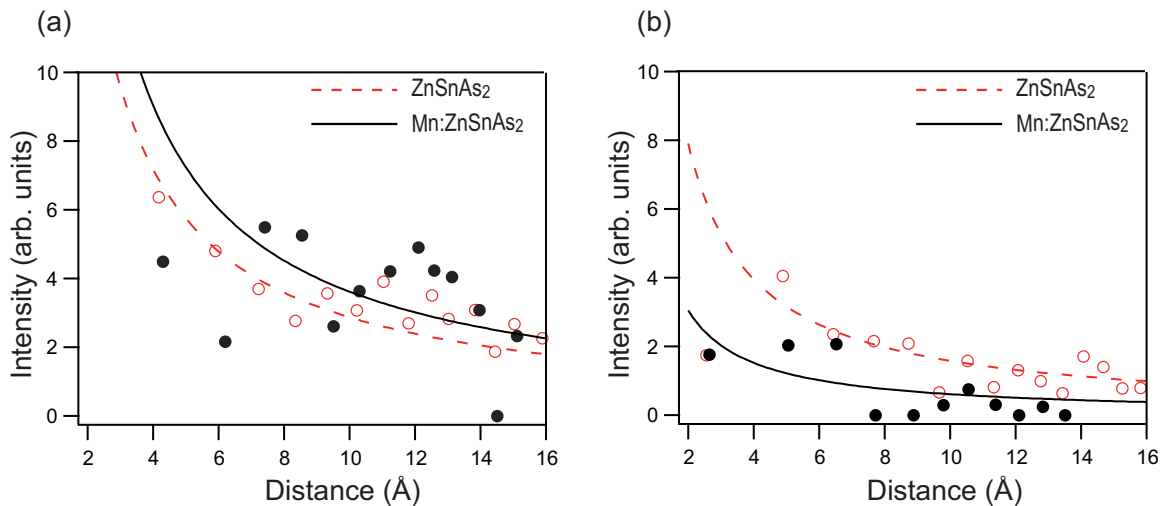


FIG. 3. Intensities of the (a) cation and (b) anion atomic images as a function of the distance from the origin. The filled and open circles indicate the intensities from $(\text{Zn, Mn, Sn})\text{As}_2$ and ZnSnAs_2 , respectively. The dashed and solid lines indicate the fitting curves for $(\text{Zn, Mn, Sn})\text{As}_2$ and ZnSnAs_2 , respectively. All intensities are normalized to the atomic numbers of the elements.

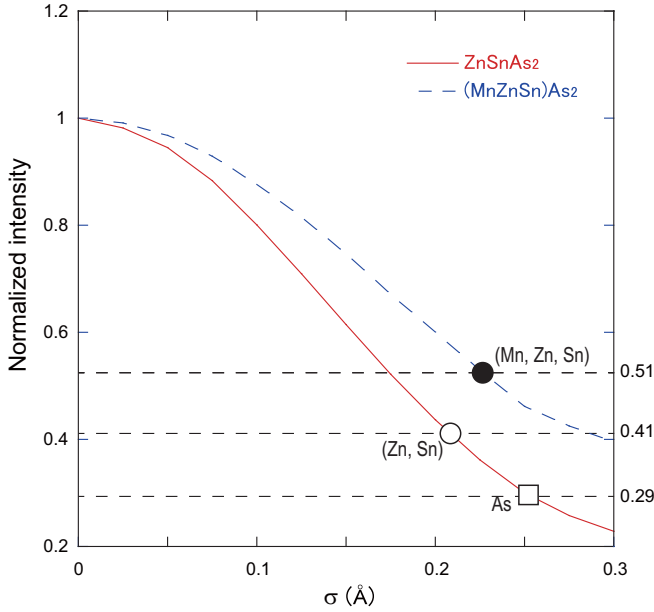


FIG. 4. σ dependence of the atomic image intensity on the atomic positional fluctuation for ZnSnAs_2 (solid curve) and $(\text{Zn, Mn, Sn})\text{As}_2$ (dashed curve). The intensity is normalized to their highest value at $\sigma = 0 \text{ \AA}$. Open circles and squares indicate the cation and anion image intensities in ZnSnAs_2 , respectively. Filled circle indicates cation image intensity in $(\text{Zn, Mn, Sn})\text{As}_2$.

sity varies by the number of holograms and the x-ray energy range used in the measurement. Therefore, we calculated the holograms of $(\text{Zn, Sn, Mn})\text{As}_2$ and ZnSnAs_2 with different energy ranges 9.8-10.8 keV (0.5 keV steps) and 9.8-13.3 keV (0.25 keV steps), respectively. These energy ranges and steps are the same as those used in the XFH experiments for $(\text{Zn, Sn, Mn})\text{As}_2$ and ZnSnAs_2 [12], respectively. Then we corrected the experimental image intensities by dividing by the atomic image intensities obtained from the calculated holograms. Such data processing is essential for estimating pure fluctuation effects.

IV. DISCUSSION

A. Estimation of atomic fluctuations from the reconstructions

In principle, the atomic image intensity is inversely proportional to the distance from the emitter [13]. Therefore, the intensity variations, shown in Figs. 3(a) and 3(b), were fitted by the simple formula a/d , where d is the distance from the central Mn or Zn atom and a is a fitting parameter, giving the positional stabilities of the atoms. Since some specific short-range correlations were observed for near-neighboring atoms [13], the fitting was carried out in a far distance range of 6-16 \AA . We obtained a values 36.16 ± 2.43 for cations in $(\text{Zn, Sn, Mn})\text{As}_2$, and 29.55 ± 3.18 for cations in ZnSnAs_2 .

The atomic image intensity can be further reduced by the fluctuations in the atomic position [12]. Figure 4 shows the intensity variations as a function of σ , which is the mean square displacement of the neighboring scatterer atom relative to the central emitter atom. Dashed and solid curves correspond to the σ dependences of the intensity variations

obtained from the simulated holograms with the energy ranges of 6.8-10.8 and 9.8-13.3 keV, respectively. The intensities are normalized with their highest values. As seen in Fig. 4, the intensity decays more rapidly in the solid curve obtained from the higher-energy holograms. In the previous study, we estimated $\sigma_{\text{Zn-C}} = 0.207 \text{ \AA}$ and $\sigma_{\text{Zn-As}} = 0.255 \text{ \AA}$ for the ZnSnAs_2 sample [12], and these values correspond to the normalized intensities of 0.41 and 0.29 on the solid curve in Fig. 4, respectively. In principle, the normalized intensity is proportional to the a value. From the ratio of a between $(\text{Zn, Sn, Mn})\text{As}_2$ and ZnSnAs_2 , we can know that the normalized intensity of the cations in $(\text{Zn, Sn, Mn})\text{As}_2$ is 0.52 on the dashed curve. Then we obtained $\sigma_{\text{Mn-C}} = 0.226 \text{ \AA}$, which is slightly larger than $\sigma_{\text{Zn-C}}$. This means that the cation sublattice is still stable even with Mn doping. On the other hand, for the anion (As), the a value is 0.42 for $(\text{Zn, Sn, Mn})\text{As}_2$, and we obtained the normalized intensity of 0.11. This value is too small to estimate σ , which must be larger than 0.4 \AA .

In Fig. 3(a), the intensities of first nearest neighbor (1NN) and second nearest neighbor (2NN) cation images are significantly smaller than the fitting curve, suggesting local fluctuations of the cation sublattice around Mn. To evaluate the local fluctuations from another point of view, we plotted the cross sections of the atomic images of Fig. 2(a) along the $\langle 110 \rangle$ and $\langle 100 \rangle$ axes as shown in Figs. 5(a) and 5(b), respectively. It can be seen in Fig. 5 that the images of the 1NN and 2NN cations are broader than the other ones, indicating larger fluctuations of these cations due to the extent of local lattice distortion around Mn up to $\sim 6 \text{ \AA}$. For comparison, we also show the image cross sections of ZnSnAs_2 in Figs. 5(c) and 5(d), where no atypical features are seen in the intensity and widths of the first and second neighbor cation images.

The peak intensities and widths of all atomic images in Fig. 5 were analyzed by fitting with the Gaussian function. Figure 6 shows the plots of the obtained values. Solid and open circles indicate the intensities and the widths of these peaks, respectively. The horizontal dashed lines in the graphs indicate $\sigma_{\text{Mn-C}}$ and $\sigma_{\text{Zn-C}}$, respectively, which are slightly lower than the peak widths of the images above 6 \AA . In Fig. 6(b), all the intensities are close to the curved dashed lines, which indicate the expected intensities, while, for $(\text{Zn, Sn, Mn})\text{As}_2$, the 1NN and 2NN in Fig. 6(b) peaks are weaker than the expected intensities, and they are broader than the succeeding atoms. These results indicate that $(\text{Zn, Sn, Mn})\text{As}_2$ certainly includes local fluctuations of the cation sublattice, while the ZnSnAs_2 thin film does not. This is most clearly observed in the 2NN atomic images.

B. Theoretical verification for the atomic fluctuations

To discuss the anomaly in the fluctuations of 2NN atoms, we calculated forces acting on positionally fixed Mn^\uparrow , Mn^\downarrow , Zn, and Sn atoms after the structural optimization using the DFT calculations of chalcopyrite $(\text{Zn, Sn, Mn})\text{As}_2$, as shown in Fig. 7. Similar trends are seen for Mn and Sn; that is, the first and second largest forces are found at the 2NN and 1NN, respectively. Surprisingly, this shell dependence agrees well with that of the broadness of the atomic images in Fig. 6(a). For Zn, the maximum of the force appears at 1NN, but the trend on the other shells is the same as those of Mn and

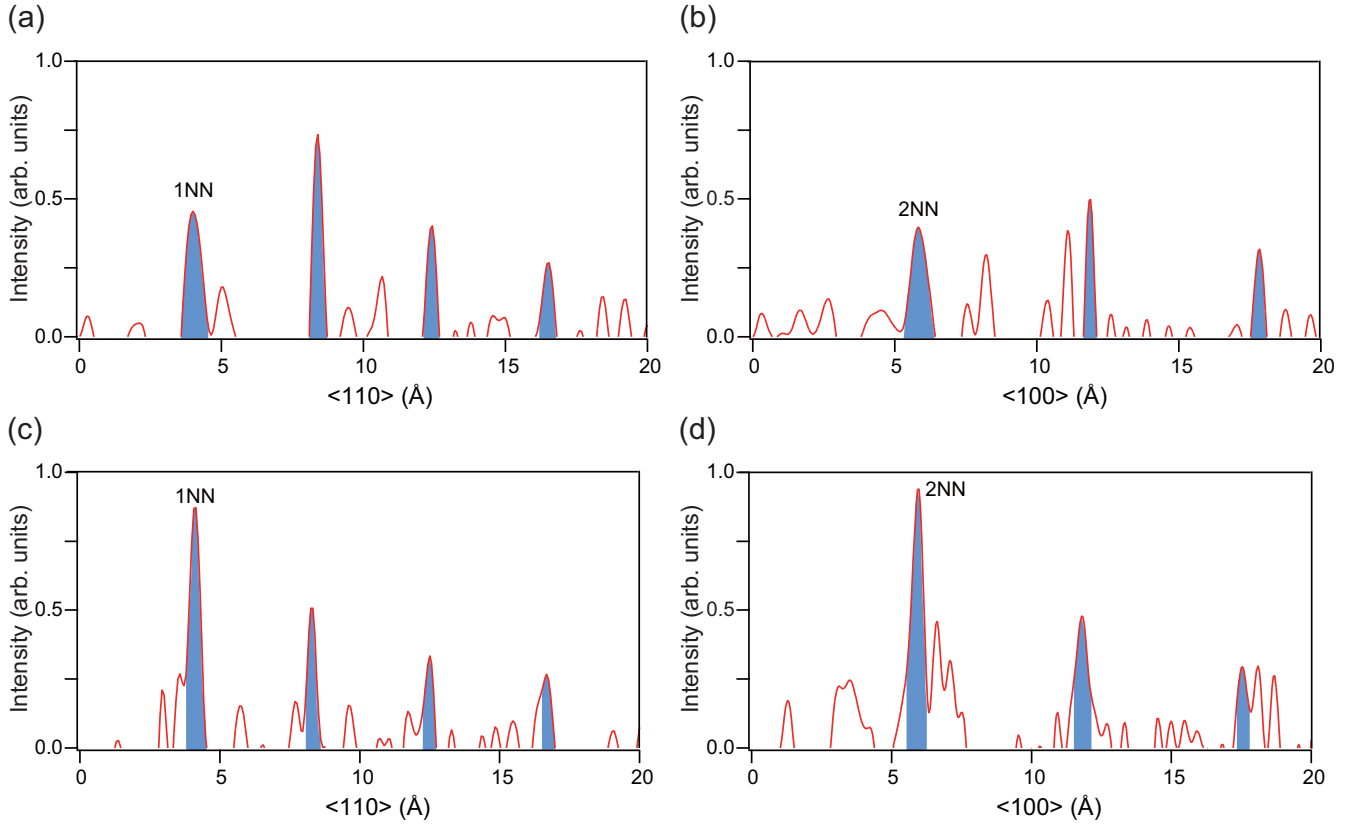


FIG. 5. Cross sections of the atomic images along (a), (c) $\langle 110 \rangle$ and (b), (d) $\langle 100 \rangle$ directions. (a), (b) indicates $(\text{Zn, Sn, Mn})\text{As}_2$. (c), (d) indicates ZnSnAs_2 .

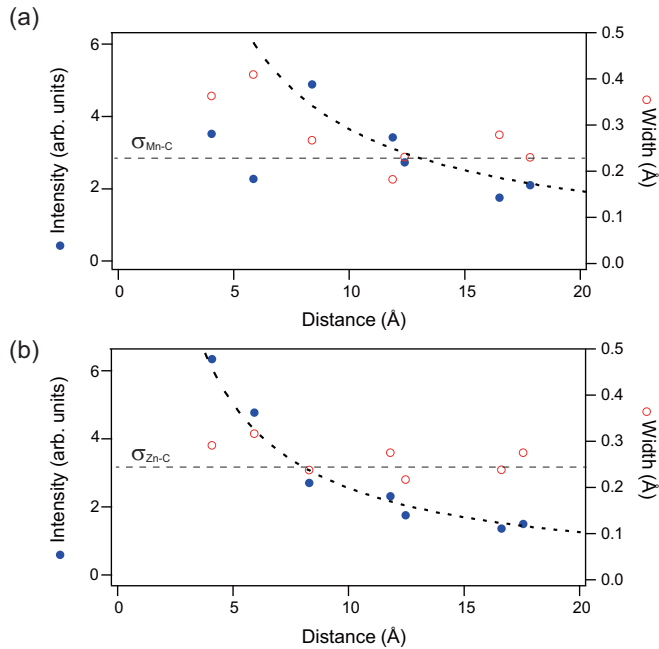


FIG. 6. Intensities and widths of the atomic images as functions of distance from the origins. (a), (b) represent atomic images around Mn in $(\text{Zn, Mn, Sn})\text{As}_2$ and Zn in ZnSnAs_2 , respectively. Guides for the eye are depicted as dashed lines, which are the same curves in Fig. 3(a). Open and filled circles indicate the widths and intensities of the atomic images, respectively.

Sn. The similarity between Mn and Sn is attributed to the hybridization between Mn- d and Sn- p states in the valence bands, as shown in the Supplemental Material [22] (see Fig. S2). Among the constituent cations, the behavior of Sn should most significantly affect the experimental atomic images considering the large atomic number and the large fraction. To distinguish the contributions of each element to the broadening of the atomic images, we estimated the forces along the radial and angular directions indicated by the inset of Fig. 7(a), and tabulated their values for 1NN and 2NN cations under the FM state, as shown in Table I. The magnitudes of these forces are shown in Fig. 7(b) for visual comprehension.

In principle, the forces in the radial direction would result in the attraction ($-z$) or repulsion (z) of the target atom, while

TABLE I. Forces along the radial and angular directions on Mn, Zn, and Sn atoms for 1NN and 2NN cation sites for the FM state. λ indicates the angle between the respective force and vector coordinates from Mn to X atoms ($X = \text{Mn, Zn, and Sn}$).

	Radial (meV/Å)	Angular (meV/Å)	λ (deg)
Mn-1NN	-1.445	4.473	107.9
Zn-1NN	-5.174	6.002	130.8
Sn-1NN	-0.661	1.144	120.0
Mn-2NN	-0.013	12.50	90.1
Zn-2NN	6.343	0	0
Sn-2NN	0.013	5.643	89.9

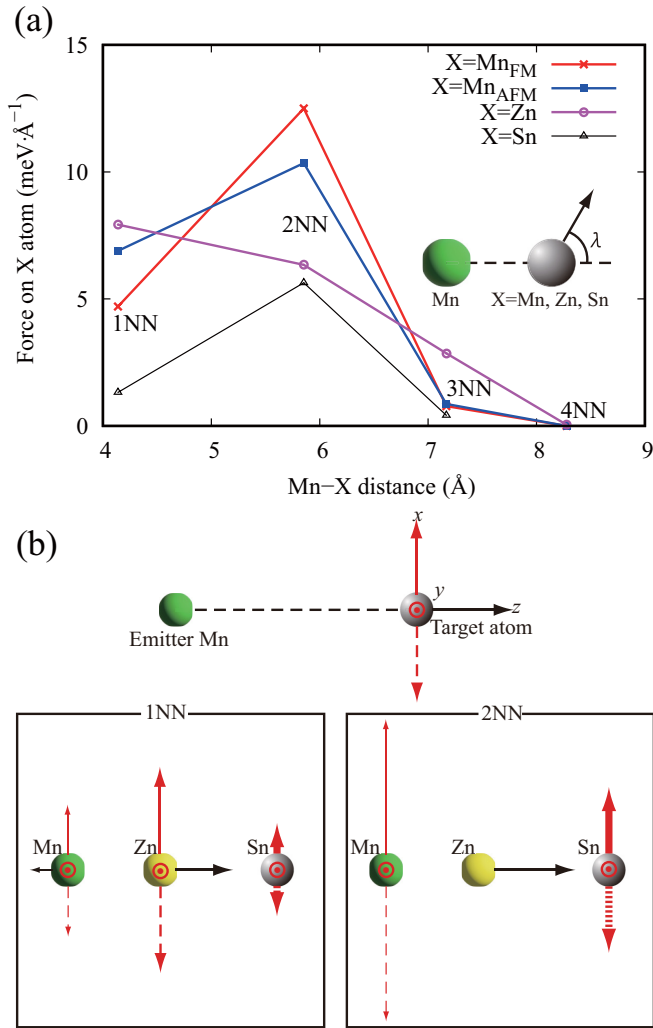


FIG. 7. Forces acting on the X atoms ($X = \text{Mn}_{\text{FM}}$, Mn_{AFM} , Zn, and Sn). (a) Plot of the calculated forces as a function of Mn-X interatomic distance. (b) Illustration of radial (black) and angular (red) forces on X for 1NN (left) and 2NN (right). The length of the arrow line indicates the magnitude of force. The thickness indicates the product of the atomic number and the fraction of the target element, which is basically proportional to the intensity of the atomic image.

the forces in the angular direction correspond to the splitting or broadening of the atomic images, because there are four equivalent directions (x , $-x$, y , $-y$) for the displacements of atoms. If the displacement is too large (>0.2 Å) or too wide (>0.3 Å FWHM), the atomic image will be rather broadened. First, let us see the forces on Zn and Sn in the radial direction in Fig. 7(b). Here, the forces on Mn are ignored due to its low concentration and small atomic number. Since the forces on Sn atoms at both the 1NN and 2NN sites are negligible, they would stay along the radial direction. Since the force on Zn-2NN is larger than that on 1NN, the displacement magnitude along the radial direction would be also larger. If the stationary Sn and the displaced Mn mainly constructed the atomic image, the 2NN image is likely to be broader for this reason. On the other hand, along the angular direction, Zn-1NN exhibits slightly larger values than Sn-2NN. However, since the atomic number of Sn is ~ 1.7 times larger than that

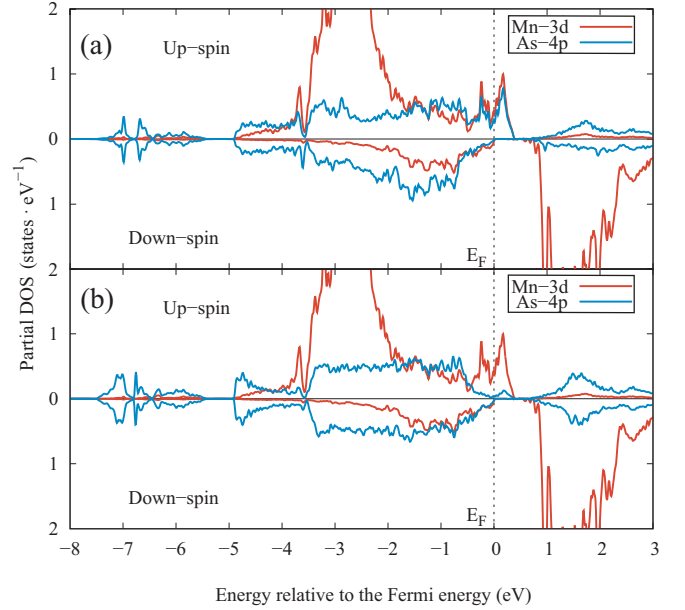


FIG. 8. Calculated partial density of d states at the Mn site (red solid lines) and that of p states at As site (blue solid lines) for (a) neighboring and (b) 3NN anion site being apart from the Mn atom in $\text{Zn}(\text{Sn}_{0.9375}, \text{Mn}_{0.0625})\text{As}_2$ in the FM state, respectively. The horizontal axis depicts the energy relative to the Fermi energy.

of Zn, the contribution of Sn to the image broadening should be greater. Therefore, the analysis of angular force can also explain the reason why the 2NN atomic image is broadened. Although the reproduction of the atomic fluctuation, which is directly related to the image broadening, was difficult with DFT calculation, we could explain qualitatively the anomaly of the 2NN atoms using the calculated forces, as mentioned above.

C. Relation between magnetism and atomic coordinates

The large As-sublattice distortion near the Mn atoms may be related to the room-temperature ferromagnetism of this system. Analysis of the atomic image intensities in Fig. 4 suggests that the As sublattice in $(\text{Zn}, \text{Sn}, \text{Mn})\text{As}_2$ is further distorted by ~ 0.4 Å from the initially distorted lattice of the pure sphalerite ZnSnAs_2 [12]. Our first-principles calculation with full structural optimization showed that the Mn-As nearest neighbor atomic distance is 2.483 Å, which is 0.177 Å shorter than the Zn-As nearest neighbor distance in ZnSnAs_2 . On the other hand, the atomic positions of As, which are more than third nearest neighbor (3NN) away from Mn, converged within 0.016 Å to approximately the same positions as that in ZnSnAs_2 . These results indicate that doping of Mn induces additional large distortions of the As sublattices around the Mn atoms. The extent of localized distortion is limited to the first and second neighboring As atoms from Mn.

Figure 8 shows the partial density of states (DOS) of the Mn-3 d states and the As-4 p states, comparing the Mn-DOS with the As-DOS calculated for the As site at the 1NN and the 3NN coordinates from Mn. The DOS of the Mn d band shows a considerable exchange splitting of ~ 4 eV, representing the ferromagnetic state of Mn. Mn has a significant

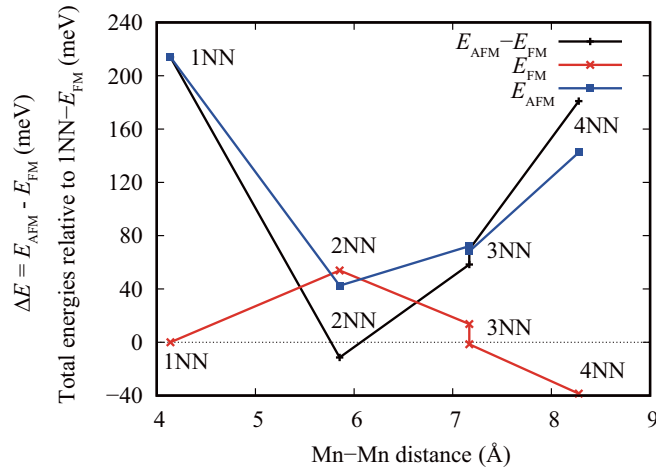


FIG. 9. Total energies, E_{FM} and E_{AFM} , under ferromagnetic and antiferromagnetic conditions relative to that of 1NN- E_{FM} as a function of Mn-Mn distance. Here, the total energy of 1NN- E_{FM} is used as the reference value, and the relative energies from the reference are plotted. The energy difference, $\Delta E = E_{\text{AFM}} - E_{\text{FM}}$, indicates the stability of ferromagnetism.

up-spin density near the Fermi level (E_F), i.e., $E_F - 0.5 < E < E_F + 0.5$ eV, and a negligibly small density in the down-spin band, indicating the half-metal nature of $(\text{Zn}, \text{Sn}, \text{Mn})\text{As}_2$. In Fig. 8(a), the up-spin band of 1NN-As has a large DOS near E_F , which is quite similar to the DOS of the Mn d band, while the down-spin counterpart at E_F has almost zero. This suggests that the p band of 1NN-As is spin polarized due to p - d hybridization, which contributes to spin-polarized transport mediated by hole spin in terms of the p - d exchange mechanism [4]. On the contrary, for As at the 3NN coordinates shown in Fig. 8(b), the DOS in the up-spin near E_F becomes very small. This result indicates that p - d hybridization in the Mn-As pair in the 3NN coordinates is weak. In addition, another calculation for ZnSnAs_2 suggested that the Zn semicore d and As p orbitals are hardly mixed in Zn-As pairs of 1NN and 3NN coordinates compared with the Mn-As system.

From these results, the larger As-sublattice distortion in $(\text{Zn}, \text{Sn}, \text{Mn})\text{As}_2$ compared with that of ZnSnAs_2 could be caused by the stable p - d exchange mechanism around Mn [23,24]. This enables us to dope over 5% Mn into ZnSnAs_2 without any magnetic secondary phases because the As-sublattice distortion plays the role of a cushion layer. Such a synergetic effect would give rise to the room-temperature ferromagnetism in $(\text{Zn}, \text{Sn}, \text{Mn})\text{As}_2$. It would be useful to perform x-ray magnetic circular dichroism (XMCD) spectroscopy at the As K edge to verify the polarization of the As $4p$ band.

Finally, to discuss the enhanced ferromagnetism in $(\text{Zn}, \text{Sn}, \text{Mn})\text{As}_2$, magnetic stability was investigated, as shown in Fig. 9. The total energy difference between FM and AFM states, ΔE , shows the stability of the FM state in this system, and it significantly varies by the Mn-Mn distance. Basically, the FM order is more stable than AFM order except for a system of 2NN, but still ΔE is only slightly less than zero. This tendency is similar to the theoretical results by

Oomae *et al.* [30]. Since the ΔE is largest at 1NN, Mn-As-Mn configuration would prefer to go ferromagnetic. On the other hand, although ΔE at fourth nearest neighbor (4NN) is also large, it would be somewhat overestimated by double counting effects due to the boundary condition used. The anomaly in magnetism was again seen in the 2NN configuration, like the large fluctuation of 2NN atoms. In Fig. 7, the force on Mn is maximized at the 2NN mainly due to the magnetic interaction between two Mn atoms, which could enhance the Mn fluctuation and thus indirectly increase the image broadening even if Mn concentration is low.

Our calculations also suggest that the magnetic coupling between the Mn atoms in the 2NN configuration can be either FM or AFM. Therefore, its presence does not contribute to the ferromagnetism of the $(\text{Zn}, \text{Sn}, \text{Mn})\text{As}_2$ of the sample. If the Mn doping site is completely controlled during the sample growth process so that the number of 2NN Mn configurations is significantly reduced, one will enhance the ferromagnetism and thus increase the T_C . This is a great technical challenge, but even with the current MBE technique, it may be possible to create a sample structure that does not contain 2NN Mn pairs in the thickness direction of the film.

V. CONCLUSION

We presented XFH results on the local atomic structure around Mn in a $(\text{Zn}, \text{Sn}, \text{Mn})\text{As}_2$ thin film, and verified them with DFT calculations. The reconstructed 3D atomic images showed a sphalerite structure with a significantly distorted As sublattice, the reason for which was the shortening of the Mn As bond length due to the p - d exchange mechanism. The As-sublattice distortion allows high doping of Mn, and the p - d exchange coupling between Mn and As preserves the entire ferromagnetism. Such a synergistic effect gives rise to the room-temperature ferromagnetic semiconductor of $(\text{Zn}, \text{Sn}, \text{Mn})\text{As}_2$. We also found anomalies in the positional fluctuations at the 2NN cations from the reconstructed atomic images. Our DFT study indicated that the forces acting on 2NN cations were stronger than those at other shells, which would produce the extraordinary positional fluctuations. The 2NN Mn-Mn configuration also showed the anomaly in FM and AFM stabilities, which will give way to fabricating unique ferromagnetic semiconductors.

ACKNOWLEDGMENTS

This experiment was performed at BL39XU of SPring-8 (Proposals No. 2010A1173 and No. 2011A1270). This work was supported by the Japan Society for the Promotion of Science (JSPS) with Grant-in-Aids for Scientific Research on Innovative Areas “3D Active-Site Science” (Grants No. 26105006 and No. 26105010), for Transformative Research Areas (A) “Hyper-Ordered Structures Science” Grants No. 20H05878 and No. 20H05881, and Scientific Research (A) (19H00655). One of the authors (N.U.) thanks the students of N.U.’s laboratory for their technical support on the present work. We thank Prof. Y. Morikawa, Osaka University, for providing us with his computational environment.

- [1] S. Datta and B. Das, *Appl. Phys. Lett.* **56**, 665 (1990).
- [2] G. Schmidt, D. Ferrand, L. W. Molenkamp, A. T. Filip, and B. J. van Wees, *Phys. Rev. B* **62**, R4790(R) (2000).
- [3] T. Dietl and H. Ohno, *Rev. Mod. Phys.* **86**, 187 (2014).
- [4] K. Sato, L. Bergqvist, J. Kudrnovský, P. H. Dederichs, O. Eriksson, I. Turek, B. Sanyal, G. Bouzerar, H. Katayama-Yoshida, V. A. Dinh, T. Fukushima, H. Kizaki, and R. Zeller, *Rev. Mod. Phys.* **82**, 1633 (2010).
- [5] T. Jungwirth, J. Sinova, J. Mašek, J. Kučera, and A. H. MacDonald, *Rev. Mod. Phys.* **78**, 809 (2006).
- [6] M. Tanaka, S. Ohya, and P. N. Hai, *Appl. Phys. Rev.* **1**, 011102 (2014).
- [7] G. A. Medvedkin, T. Ishibashi, T. Nishi, K. Hayata, Y. Hasegawa, and K. Sato, *Jpn. J. Appl. Phys.* **39**, L949 (2000).
- [8] S. Choi, G.-B. Cha, S. C. Hong, S. Cho, Y. Kim, J. B. Ketterson, S.-Y. Jeong, and G.-C. Yi, *Solid State Commun.* **122**, 165 (2002).
- [9] J. T. Asubar, Y. Jinbo, and N. Uchitomi, *J. Cryst. Growth* **311**, 929 (2009).
- [10] N. Uchitomi, J. T. Asubar, H. Oomae, H. Endoh, and Y. Jinbo, *e-J. Surf. Sci. Nanotechnol.* **9**, 95 (2011).
- [11] M. Tegze and G. Faigel, *Nature (London)* **380**, 49 (1996).
- [12] K. Hayashi, N. Uchitomi, K. Yamagami, A. Suzuki, H. Yoshizawa, J. T. Asubar, N. Happo, and S. Hosokawa, *J. Appl. Phys.* **119**, 125703 (2016).
- [13] S. Hosokawa, N. Happo, T. Ozaki, H. Ikemoto, T. Shishido, and K. Hayashi, *Phys. Rev. B* **87**, 094104 (2013).
- [14] W. Hu, K. Hayashi, T. Yamamoto, N. Happo, S. Hosokawa, T. Terai, T. Fukuda, T. Kakeshita, H. Xie, T. Xiao, and M. Suzuki, *Phys. Rev. B* **80**, 060202(R) (2009).
- [15] S. Marchesini, F. Schmithüsen, M. Tegze, G. Faigel, Y. Calvayrac, M. Belakhovsky, J. Chevrier, and A. S. Simionovici, *Phys. Rev. Lett.* **85**, 4723 (2000).
- [16] K. Hayashi, N. Uchitomi, J. T. Asubar, N. Happo, W. Hu, S. Hosokawa, and M. Suzuki, *Jpn. J. Appl. Phys.* **50**, 01BF05 (2011).
- [17] T. Gog, P. M. Len, G. Materlik, D. Bahr, C. S. Fadley, and C. Sanchez-Hanke, *Phys. Rev. Lett.* **76**, 3132 (1996).
- [18] J. J. Barton, *Phys. Rev. Lett.* **67**, 3106 (1991).
- [19] P. Giannozzi, S. Baroni, N. Bonini, M. Calandra, R. Car, C. Cavazzoni, D. Ceresoli, G. L. Chiarottia, M. Cococcioni, I. Dabo, A. D. Corso, S. Fabris, G. Fratesi, S. de Gironcoli, R. Gebauer, U. Gerstmann, C. Gougoussis, A. Kokalj, M. Lazzeri, L. Martin-Samos *et al.*, *J. Phys.: Condens. Matter* **21**, 395502 (2009).
- [20] D. Gasson, P. Holmes, I. Jennings, B. Marathe, and J. Parrot, *J. Phys. Chem. Solids* **23**, 1291 (1962).
- [21] D. F. Shanno and K.-H. Phua, *Math. Program.* **14**, 149 (1978).
- [22] See Supplemental Material at <http://link.aps.org/supplemental/10.1103/PhysRevB.106.064434> for (i) a crystal structure used in first-principles calculations and (ii) calculated density of states at cation sites in Zn(Sn, Mn)As₂.
- [23] H. Kizaki and Y. Morikawa, *Jpn. J. Appl. Phys.* **57**, 020306 (2018).
- [24] H. Kizaki and Y. Morikawa, *Jpn. J. Appl. Phys.* **58**, 110601 (2019).
- [25] S. Hidaka, H. Toyota, and N. Uchitomi, *Appl. Phys. Lett.* **110**, 132410 (2017).
- [26] J. T. Asubar, A. Kato, Y. Jinbo, and N. Uchitomi, *Jpn. J. Appl. Phys.* **47**, 657 (2008).
- [27] N. Happo, K. Hayashi, S. Senba, H. Sato, M. Suzuki, and S. Hosokawa, *J. Phys. Soc. Jpn.* **83**, 113601 (2014).
- [28] S. Hosokawa, N. Happo, and K. Hayashi, *Phys. Rev. B* **80**, 134123 (2009).
- [29] H. Wen, K. Hayashi, T. Fukumura, K. Akagi, M. Tsukada, N. Happo, S. Hosokawa, K. Ohwada, M. Takahashi, M. Suzuki, and M. Kawasaki, *Appl. Phys. Lett.* **106**, 222403 (2015).
- [30] H. Oomae, M. Shinoda, J. T. Asubar, K. Sato, H. Toyoda, N. Mayama, B. Mehdiyev, and N. Uchitomi, *J. Appl. Phys.* **125**, 073902 (2019).